A Dual Inhibitory Network in the Thalamic Reticular Nucleus Delineated by Pallidal and Intra-Reticular Inhibition

Authors: Frances S. Cho[1,2,3+], John R. Huguenard[4], Jeanne T. Paz[1,2,3]*

Affiliations:

[1] Gladstone Institute of Neurological Disease, Gladstone Institutes, San Francisco CA 94158

[2] Department of Neurology, University of California San Francisco, San Francisco CA 94158

[3] Kavli Institute for Fundamental Neuroscience, University of California San Francisco, San Francisco CA 94158

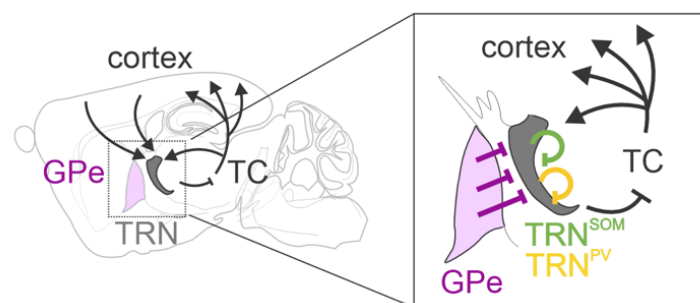[4] Department of Neurology & Neurological Sciences, Stanford University School of Medicine, Stanford CA 94305

[+]Current affiliation: Department of Neurobiology, Stanford University School of Medicine, Stanford CA 94305

Keywords: Thalamic Reticular Nucleus (TRN); External Globus Pallidus (GPe); GABAergic inhibition; Inhibitory Circuit Motifs; Counter-Inhibition and Feed-Forward Circuit Motifs.

Declaration of Interests: The authors have no competing interests to declare.
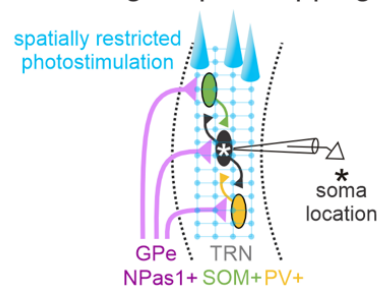
ABSTRACT

Long described as an inhibitory "guardian of the gateway," the thalamic reticular nucleus (TRN) shapes which thalamic signals reach the cortex during attention, arousal, and sensory processing. However, how the inhibitory wiring within TRN supports this flexible gating—from modality-specific tuning to global control—remains poorly defined. Using cell type–specific optogenetic input mapping and whole-cell patch-clamp recordings in mice, we dissect inhibitory connectivity in TRN from two major GABAergic sources: the TRN itself and the external globus pallidus (GPe). All recorded TRN neurons received inhibition from the GPe, whereas a subset also received intra-TRN inhibition. Intra-TRN inhibition arose predominantly from somatostatin-expressing onto parvalbumin-expressing TRN neurons (SOM→PV), revealing subtype-specific connectivity recruited by thalamic excitation to form a feedforward motif. These findings delineate a dual inhibitory architecture: local intra-TRN circuits provide spatially selective inhibition, whereas pallidal inputs deliver diffuse inhibition. These complementary mechanisms may support both modality-specific gating and global state-dependent control of thalamic output.

Graphical Abstract: The thalamic reticular nucleus (TRN) integrates two distinct inhibitory motifs. Sparse, dendrite-targeting intra-TRN connections from parvalbumin- and somatostatin-expressing neurons provide structured, feedforward inhibition recruited by thalamocortical (TC) inputs. In parallel, robust and widespread inhibition from Npas1-expressing neurons of the external globus pallidus (GPe) supplies a strong external drive that can coordinate activity across the TRN. Together, these complementary motifs define a dual inhibitory architecture that may shape thalamocortical gating and highlight cellular entry points for therapeutic intervention.

Introduction

The thalamic reticular nucleus (TRN) is a central inhibitory hub that gates thalamocortical communication and regulates attention, arousal, and sensory processing[1–5]. Comprised entirely of GABAergic neurons, the TRN exerts powerful inhibition onto thalamic relay nuclei, yet the organization of inhibition within the TRN itself remains poorly understood[6]. The TRN contains molecularly and functionally distinct subnetworks with specialized input–output connectivity[3,7–11]. Retrograde rabies tracing identified the external globus pallidus (GPe) and the TRN itself as major GABAergic sources of input[8].

While GPe projections to TRN have been recognized for decades[12], their function has remained largely unexplored. Similarly, whether TRN neurons form chemical inhibitory synapses with one another is debated (reviewed in [4,13]). Gap junction-coupled intra-TRN electrical synapses have been consistently demonstrated by multiple groups and suggested to play a role in synchronizing TRN neurons[14–17]. However, the existence of intra-TRN chemical GABAergic synapses has been a subject of controversy, with multiple electrophysiological studies suggesting their existence and functionality in ferrets, rats, and mice[16,18,19], and others failing to find them[20–22]. This controversy highlights the need for systematic analysis of TRN inhibitory connectivity across molecularly defined subtypes and comparison with extrinsic pallidal input. Understanding how these inhibitory motifs are organized is critical for uncovering mechanisms of thalamocortical synchrony and its disruption in conditions such as absence epilepsy, schizophrenia, and attention disorders.

Here, we dissect inhibitory connectivity within the TRN and compare it with extrinsic inputs from the GPe. Using whole-cell recordings combined with cell type–specific optogenetic input mapping in adult mice, we show that TRN neurons receive sparse, spatially organized inhibition that is mainly, but not exclusively, driven by somatostatin-expressing TRN neurons, alongside robust extrinsic input from Npas1-expressing GPe neurons. Together, these inputs define a dual inhibitory architecture that complements electrical coupling within TRN, revealing circuit motifs that may regulate thalamocortical synchrony and provide cellular entry points for therapeutic modulation in neuropsychiatric and seizure disorders.

Results

To compare extrinsic and intrinsic sources of GABAergic inhibition in TRN, we examined molecularly distinct sources of presynaptic input providing GABAergic inhibition to the TRN. We targeted GPe inputs because they represent a major source of GABAergic inhibition to TRN, with Npas1-positive GPe (GPe^{Npas}) neurons recently shown to form functional connections in the

3

48 TRN[23]. To assess intra-TRN inhibition, we examined whether somatostatin- or parvalbumin-
49 expressing TRN neurons (TRN[SOM] and TRN[PV]), the principal molecularly defined TRN
50 subpopulations[8,9,24–27], are the main sources of intra-TRN inhibition. Cre-dependent AAV-EF1α-
51 hChR2 was injected into the GPe of Npas1-Cre mice or into the TRN of Parvalbumin-Cre or
52 Somatostatin-Cre mice. Opsin expression was allowed to develop for six weeks to ensure robust
53 expression in axons. All experiments were performed in adult mice (2–7 months old).
54 Monosynaptic inputs to TRN neurons were mapped using focal (2 μm beam) photostimulation
55 with a 460 × 100 μm grid spanning the anterior-posterior axis of the TRN (**Figure 1A, Supp.**
56 **Figure 1A**). Evoked synaptic responses were easily separable from any direct photocurrent
57 based on latency and were abolished in the presence of the GABA$_A$R antagonist gabazine (see
58 Methods, **Supp. Figure 1**). Response maps were constructed by quantifying only the evoked
59 synaptic responses at sites with reliably evoked responses across multiple trials. This approach
60 enabled activation of defined GABAergic populations and mapping of their synaptic inputs onto
61 TRN neurons (**Figure 1A, Supp. Figure 1**).

62

Prevalence of Synaptic Inhibition within TRN

64 The prevalence of responses varied sharply depending on the source of inhibition. Optical
65 activation of GPe[Npas] axons in the TRN elicited inhibitory postsynaptic currents (IPSCs) in all
66 recorded TRN neurons (37/37 cells from 8 mice) (**Figure 1B**). In contrast, optical activation of
67 TRN[SOM] neurons evoked IPSCs in 18.6% of TRN neurons (17/91 cells from 17 mice), and
68 activation of TRN[PV] neurons evoked IPSCs in 8.7% (8/91 cells from 17 mice) (**Figure 1B**).
69 Because the axons in the TRN may be sparse and thin, we next investigated whether a spatially
70 larger illumination of the weakest (i.e., lowest-prevalence) presynaptic input could unmask larger
71 intra-TRN connectivity. Therefore, we stimulated TRN[PV] neurons using wider-field illumination
72 with a 200-μm optical fiber (**Supp. Figure 2A**) as opposed to a focal 2 μm beam (**Figure 1A**).
73 This wider illumination evoked monosynaptic IPSCs in 46.4% of TRN neurons (13 of 28, **Supp.**
74 **Figure 2B–C**), which we observed consistently with two distinct opsins, ChR2 (5 of 15 cells) and
75 CheTA (8 of 14) (pooled data, **Supp. Figure 2B**). The kinetics of these IPSCs were consistent
76 with prior reports and matched those observed in our focal mapping experiments (**Supp. Figure**
77 **2D–E**). In sum, the wider illumination revealed 5 times more connectivity than the focal mapping,
78 suggesting that the intra-TRN connections are sparse and likely originate from distal locations.
79 Altogether, GPe[Npas] inputs robustly inhibited all TRN neurons tested, while recurrent intra-TRN
80 synaptic inhibition originating from TRN[SOM] or TRN[PV] neurons was sparse and likely distal.

81

4

Location of TRN neurons receiving GABAergic inhibition

Because the TRN can be functionally divided into various modalities and sectors, we next asked whether the TRN neurons that receive intra-TRN versus GPe→TRN inputs are located in any specific region. TRN neurons receiving inhibition from GPe^{Npas}, TRN^{PV}, or TRN^{SOM} cellular sources were observed at every level of what was sampled along the dorsal-ventral axis. Furthermore, TRN neurons receiving inhibition were found across the entire anterior-posterior axis of the TRN (**Figure 1C**). We next characterized the distribution of TRN neurons receiving inhibition across the medio–lateral axis of the TRN by classifying the location into the TRN "core" or "shell" (with "core" defined as the central 50% along the medial–lateral axis and "shell" defined as the medial and lateral 25%, similar to previous studies[10]). Interestingly, we found that intra-TRN inputs (from TRN^{PV} or TRN^{SOM}) were enriched in the TRN "core" compared to the TRN "shell," with 16.8% of all cells recorded in the "core" (23 of 137 cells) exhibiting eIPSCs in response to photostimulation of TRN^{PV} or TRN^{SOM} inputs, compared to 3.2% prevalence of intra-TRN recipients in the "shell" (1 of 31 cells). This bias was driven by the anatomical distribution of TRN^{SOM}-recipient neurons, which had a higher prevalence in the "core" (23.5%; 16 of 52 cells) compared to the "shell" (0%; 0 of 21 cells) in Som-Cre mice. In contrast, TRN^{PV}-recipient neurons were equally likely to be found across the "core" (10.1%; 7 of 69 cells) and "shell" (10%; 1 of 10 cells) in PV-Cre mice. GPe→TRN inputs were equally likely to be found across the "core" (100%; 26 of 26 cells in Npas1-Cre mice) and the "shell" (100%; 5 of 5 cells in Npas1-Cre mice).

Spatial and Kinetic Properties of Inhibitory Synaptic Inputs to TRN

Notably, extrinsic GPe→TRN inputs versus intra-TRN inputs differed in terms of their amplitude and kinetics. When comparing the kinetics of eIPSCs at the maximally active photostimulation site, eIPSCs evoked by GPe^{Npas} inputs were twofold larger in amplitude and two to threefold longer in half-width than those from TRN^{PV} or TRN^{SOM} neurons (**Figure 2K–L**). To investigate if these differences could be driven by the spatial location of GPe→TRN versus intra-TRN inputs (e.g., proximal or distal to the postsynaptic cell body), we turned to high-resolution focal photostimulation to map the afferent inputs.

Both GPe^{Npas}→TRN and intra-TRN–evoked IPSCs could be driven by activating sites up to 300 μm away from the postsynaptic cell body along the anterior–posterior axis, and up to ~80 μm away along the medial–lateral axis (**Figure 2A–H**). Moreover, intra-TRN-recipient and GPe-recipient neurons exhibited a similar fraction of "effective" sites in the photostimulation protocol, indicating that both groups displayed a similarly high density of afferent connectivity (**Figure 2I**, **Supp. Figure 1C–D**).

5

116   For a subset of "responder" cells, we also mapped synaptic inputs with higher resolution closer to the cell body (66 × 66 µm grid) around the cell body (22 µm spacing), compared to a 460 × 100 µm grid (33 µm spacing). For brevity, we refer to these as microscale (<100 µm) and mesoscale (>100 µm) maps. We observed a striking difference across the distinct sources of inhibition when comparing synaptic responses evoked by microscale versus mesoscale inputs. Among GPe-recipient TRN responder cells, 90.9% (10 of 11 cells) displayed eIPSCs triggered by focal photostimulation using both micro- and meso-scale maps, suggesting that effective Npas1$^+$ inputs were located both proximal and distal to the cell body. In contrast, only 28.5% of TRN^{PV}-recipient neurons (2 of 7 cells) and TRN^{SOM}-recipient neurons (4 of 14 cells) displayed eIPSCs triggered by focal photostimulation at both micro- and meso-scale maps. In other words, the majority of intra-TRN inhibitory connectivity was observed exclusively with meso-scale maps which primarily activate inputs distal to the cell body (71.5%; 6 of 21 cells), while GPe→TRN inhibitory connectivity was similarly recruited across micro- and meso-scale maps. Altogether, these results suggest that although intra-TRN recipient cells may be sparse, they display robust, wide-ranging afferent connectivity that is comparable to that observed in GPe^{Npas}→TRN responder cells. However, GPe^{Npas} inputs provided stronger and longer-lasting inhibition in contrast to local TRN^{PV} and TRN^{SOM} inputs, demonstrating an intriguing dissociation between extrinsic versus local sources of inhibition.

Rules of Intra-TRN Connectivity

136 TRN neurons are characterized by distinct molecular and electrophysiological hallmarks and are embedded in distinct neural circuits[8,9]. In light of this heterogeneity, we next investigated if subnetworks are preferentially engaged in recurrent inhibition within the TRN by leveraging the fact that PV and SOM are neurochemical markers of two major classes of TRN neurons[8,9,27]. Although we were unable to recover the neurochemical marker of each responder cell using immunohistochemistry, we used the presence of a direct ChR2-evoked photocurrent in the postsynaptic cell as a proxy for the whether the cell was transgene-positive or negative (i.e., TRN^{PV+}, TRN^{PV-}, TRN^{SOM+}, or TRN^{SOM-} neurons). Based on prior literature, we assumed that Som-negative TRN cells are likely PV-positive[8,10]. ChR2-evoked photocurrents were distinguishable from synaptic responses due to their fast latency relative to laser onset and their persistence in the presence of gabazine in a subset of cells (**Supp. Figure 1B**).

147   In Som-Cre mice, only 1 of 17 TRN^{SOM}-recipient TRN neurons exhibited direct photocurrents in response to photostimulation, suggesting that TRN^{SOM+} typically do not receive intra-TRN inputs from other TRN^{SOM+} neurons (i.e., reciprocal connections between TRN^{SOM}

150   neurons are rare). Among the remaining 16 TRN^{SOM}-recipient TRN neurons which failed to exhibit

151   direct photocurrents, 100% were located in the TRN core (15 of 15 cells for which we were able

152   to reconstruct the anatomical location). Given that the core and shell are predominantly populated

153   by TRN^{PV} and TRN^{SOM} neurons, respectively,[8,10] together with the absence of direct photocurrents

154   in nearly all responders, we infer that the majority of TRN^{SOM}-recipient TRN neurons have a high

155   likelihood of being TRN^{SOM-}. Taken together, these results reveal a dominance of

156   TRN^{SOM+}→TRN^{SOM-} connectivity (94.1% of responders) relative to TRN^{SOM+}→TRN^{SOM+}

157   connectivity (5.9% of responders). In PV-Cre mice, we classified 3 of 8 TRN^{PV}-recipient TRN

158   neurons as putative TRN^{PV+} neurons based on the presence of a direct photocurrent and

159   anatomical location in the TRN core. These observations suggest a similar probability of

160   TRN^{PV+}→TRN^{PV+} connectivity (37.5% of responders) relative to TRN^{PV+}→TRN^{PV-} connectivity

161   (62.5% of responders), although generally, it was very rare for TRN^{PV} to be a presynaptic source

162   of intra-TRN inhibition given the lower prevalence of responder cells when stimulating TRN^{PV}

163   inputs (8.7%) compared to stimulating TRN^{SOM} inputs (18.6%). Taken together, these

164   observations start to elucidate the rules of intra-TRN connectivity by establishing which pre-

165   postsynaptic connections are possible.

166

Feed-Forward Recruitment of Inhibition

168   The TRN is a critical component of corticothalamic feed-forward inhibition (CT→TRN→TC) and

169   feed-back inhibition (TC→TRN→TC) of TC neurons. However, whether excitatory inputs to TRN

170   can recruit intra-TRN inhibition in a feed-forward manner remains unknown. To this end, we

171   injected ChR2-expressing AAV construct into the ventrobasal (VB) thalamus in adult mice under

172   the Camk2α promoter, to specifically express ChR2 in excitatory glutamatergic TC neurons in VB

173   thalamus as described[28]. Four weeks later, we prepared thalamic brain slices in which we severed

174   the connection between TRN and VB to avoid circuit reverberation (feedback inhibition in the

175   TRN→TC pathway that would cause rebound bursting in TC neurons, resulting in excitation of

176   TRN)[28]. We then investigated the effect of optogenetic activation of ChR2-expressing TC axon

177   terminals in TRN neurons (**Figure 3A–D**). Current-clamp recordings of tonic firing in TRN

178   revealed a brief increase in firing upon TC terminal activation, as expected because TC neurons

179   provide powerful excitatory input to TRN[28]. Excitation was followed by a pronounced interruption

180   of firing lasting ~200 ms before firing resumed (**Figure 3B, Supp. Figure 3**). This interruption was

181   observed reliably across multiple trials in 21.7% of TRN neurons (**Figure 3C–D**) and was

182   abolished by picrotoxin, confirming that it was mediated by GABA$_A$ receptors. Furthermore,

183   blocking AMPAR/NMDAR currents with kynurenic acid eliminated the initial firing rate increase

7

184   caused by TC activation (**Figure 3B**). Because TC neurons do not project to GPe, these inhibitory

185   effects must originate from intra-TRN connections. In summary, VB TC excitation can recruit

186   GABAergic intra-TRN inhibition, establishing a feed-forward inhibitory motif within TRN.

187

188   **Discussion**

189   ***Dual inhibitory architecture of TRN: shedding light on the "searchlight" hypothesis***

190   Together, these experiments reveal a dual inhibitory architecture of the TRN: a robust extrinsic

191   input from GPe[Npas1] neurons providing strong, uniform inhibition across the nucleus, and sparse

192   recurrent inhibition from TRN[PV] and TRN[SOM] neurons which displayed spatial selectivity and could

193   be recruited in a feed-forward manner by thalamocortical excitation. Our findings also revealed a

194   potential dissociation between the postsynaptic locations of GPe versus intra-TRN inhibitory

195   inputs. Using focal photostimulation to map connectivity at the micro- and meso-scale in the same

196   neurons, we found that GPe-recipient TRN neurons exhibited synaptic responses at both scales,

197   consistent with the presence of inhibitory inputs at both near-somatic and dendritic locations. In

198   contrast, the relative sparsity of intra-TRN inputs evoked by micro-scale mapping suggests that

199   their recruitment is biased towards more distal dendritic regions. While we did not perform

200   ultrastructural analyses or reconstruct dendritic morphology, we speculate that intra-TRN inputs

201   preferentially target distal dendrites while GPe inputs are recruited uniformly across the

202   perisomatic and dendritic domains. These patterns suggest complementary modes of synaptic

203   control by distinct inhibitory microcircuit motifs: extrinsic GPe[Npas] inputs may be well-positioned to

204   exert powerful, immediate inhibition at the soma, while recurrent intra-TRN inputs may shape

205   integration through distal dendritic inhibition.

206   Crick's "searchlight hypothesis" proposed that the TRN controls an internal attentional

207   spotlight, amplifying select thalamocortical circuits through heightened burst firing in a subset of

208   TRN neurons (Crick, 1984). Our findings refine this model by proposing two complementary

209   modes of controlling the searchlight: pallidal inputs may serve as a strong, global coordinating

210   signal that can rapidly shift TRN excitability (adjusting the "brightness" of the searchlight) while

211   intra-TRN connections may serve as mediators of structured, selective interactions (adjusting the

212   focus and location of the searchlight). Such parallel organization resembles motifs elsewhere in

213   the brain, where local and long-range inhibition interact to balance stability and flexibility. For

214   example, in hippocampal circuits, PV-expressing basket cells provide strong peri-somatic

215   inhibition while long-range projections from oriens-lacunosum moleculare (O-LM) cells inhibit

216   distal dendrites to gate excitatory inputs[29,30]. Future work should examine how intra-TRN and GPe

217   inputs are coordinated during behavior, and whether they dominate under different brain states

218   such as sleep, attention, or motor control[5].

219

220   ***Resolving intra-TRN inhibition: sparse nodes of convergence***

221   Our results provide direct functional evidence and detailed characterization of intra-TRN chemical

222   GABAergic synapses in adult mice, helping to resolve decades of conflicting reports obtained in

223   a variety of species. Early studies reported reciprocal GABAergic connections between TRN

224   neurons (e.g., see [16,18] and more recently[19], while others, mainly in mice, failed to detect them[20–

225   22]. In our hands, photostimulation of ChR2-expressing TRN[PV] neurons recruited inhibition in only

226   8.6% of TRN neurons when using focal grid stimulation (estimated 1 μm spot size), but nearly

227   50% when using wider-field photostimulation (200 μm), suggesting that intra-TRN synaptic

228   connections are distal and easily severed in slice preparations. These features would explain why

229   paired recordings—which requires both pre- and post-synaptic cell bodies to be located in the

230   same slice—or glutamate uncaging often failed to detect intra-TRN chemical inhibition, yet gap-

231   junction mediated electrical synapses are routinely detected[14,15,20] presumably because they are

232   located more proximally along dendrites than chemical synapses. Further corroborating the

233   sparse nature of intra-TRN synaptic connections, a recent study reported a single pair of TRN

234   neurons coupled via GABAergic synapses amidst hundreds of paired recordings among closely

235   apposed somata in the rat TRN[31]. Optogenetics circumvents this limitation by activating terminals

236   even when the originating soma are absent, although opsin expression in axons remains a caveat

237   in that low expression could lead to under-reporting the true prevalence. Taken together with

238   previous reports that chemical synapses in the TRN are enriched along the anterior-posterior axis

239   and follow distinct rules from electrical synapses[16], our findings support the notion that intra-TRN

240   connectivity is structured rather than uniform, and likely tailored to specific computational roles.

241   Our experiments revealed that although they may represent a small fraction of the TRN,

242   intra-TRN recipient cells nevertheless exhibit wide-ranging afferent connectivity. The sparse but

243   broadly connected nature of intra-TRN motifs suggests an intriguing, inverse analogy to "hub

244   cells" described in the hippocampus, where a sparse set of inhibitory interneurons exert

245   disproportional influence by broadcasting inhibition across a broad network [32]. Intra-TRN recipient

246   cells may represent nodes of convergence: although sparse, these TRN "convergence" cells are

247   well-positioned to gather inhibitory inputs which may be spatially distributed across distinct TRN

248   sectors and/or modalities, and subsequently gate TRN output in a state-dependent manner.

249

250

251 *Implications for TRN function*

252 Our demonstration of the relative abundance of intra-TRN GABAergic synapses, compared to

253 previous studies, expands the computational repertoire of the TRN. By providing localized,

254 dendro-dendritic inhibition, intra-TRN synapses may sharpen receptive fields, modulate

255 synchrony, and enable flexible attentional gating[4,33]. Their organization complements electrical

256 synapses, which synchronize activity within ~40 μm and occur in ~30% of TRN neurons[15,34].

257 Whereas electrical coupling synchronizes neurons within the same domain, chemical inhibition

258 may mediate lateral competition between adjacent domains or across modalities[17]. For instance,

259 lateral inhibition stabilizes one and two-dimensional attractor dynamics, giving rise to head-

260 direction selectivity in the anterior thalamus (reviewed by [35]) and the characteristic hexagonal

261 firing patterns of grid cells in the medial entorhinal cortex as rodents navigate their environments[36].

262 The recurrent inhibition within the TRN described in this study thus represents a novel circuit

263 mechanism which may endow the TRN with hitherto undescribed computational motifs.

264 Our study focused on two major subnetworks in the TRN using PV and SOM as markers.

265 While there are several other ways to parcellate TRN subpopulations using other neurochemical

266 markers (e.g., the expression of Calbindin versus Somatostatin, or Spp1 versus Ecel1[10,11], they

267 generally map onto similar delineations of TRN subnetwork in terms of their electrophysiological

268 properties and input-output connectivity. We thus consider our results to be generalizable,

269 regardless of the nomenclature of choice. Importantly, we reveal a novel interaction between two

270 subtypes of TRN neurons: although both PV and SOM neurons were capable of being pre- or

271 post-synaptic partners of intra-TRN connections, (1) PV neurons were far less likely to serve as

272 presynaptic sources of inhibition compared to SOM neurons, and (2) SOM neurons were more

273 likely to inhibit PV neurons compared to other SOM neurons, while PV neurons inhibited other PV

274 neurons and SOM neurons similarly. By revealing a previously undescribed recurrent inhibitory

275 motif between TRN neurons embedded in distinct circuits, our findings position inhibitory

276 microcircuits of the TRN as important contenders in shaping thalamocortical computations.

277

278 *Disease relevance*

279 GABAergic inhibition between TRN cells has been proposed to play a key role in constraining

280 thalamocortical synchrony[37]. Disruption of intra-TRN GABAergic transmission, whether by genetic

281 deletion of $GABA_A$ receptor β3 subunits or hemizygous loss of sodium channel encoding gene

282 *Scn8a*, produces pathological oscillations and absence seizures[19,33,37]. Moreover, loss of

283 GABAergic inhibition in TRN has been suggested to drive epileptiform discharges during sleep

284 spindles after mild brain injury[38]. Given that intra-TRN chemical and electrical synapses are likely

10

285 engaged differently across states, selective impairments could yield distinct circuit phenotypes.
286 Our work also suggests that GPe may be a stronger modulator of TRN than previously
287 appreciated, raising the possibility that dysfunction in the GPe[Npas]→TRN pathway could
288 destabilize thalamocortical rhythms, contributing to movement disorders or attentional deficits.
289 Beyond epilepsy, TRN dysfunction has been implicated in schizophrenia, Alzheimer's disease,
290 ADHD, and autism spectrum disorders, where sensory gating and attentional control are
291 impaired[39,40]. Our work dissecting the cell-type specific inhibitory microcircuits in the TRN thus
292 opens the door towards investigating specific inhibitory synapses in the TRN as potential cellular
293 targets for therapeutic interventions.

294

295 ***Limitations and future directions***
296 Although the current study focused on GPe as an external source of GABAergic inhibition to TRN,
297 there are other sources of inhibition (e.g., lateral hypothalamus[41]) for which the cell-type
298 connectivity rules are unknown. Our experiments were confined to a single spatial plane, leaving
299 unexplored potential differences along the anterior–posterior axis, which maps onto distinct
300 sensory modalities. Such mapping could clarify whether intra-TRN inhibition mediates cross-
301 modal gating, providing the synaptic substrate for Crick's "guardian of the gateway" hypothesis[42].
302 Furthermore, our experiments revealed both high and low prevalence of intra-TRN inhibition
303 depending the technique (wider-field illumination versus focal photostimulation). The true
304 prevalence likely lies between these extremes and varies with behavioral state, and characterizing
305 the extent intra-TRN recruitment in vivo will be a critical step towards illuminating the physiological
306 relevance of recurrent inhibition within the TRN.

307

308 **Methods**
309 We performed all experiments in accordance with protocols approved by the Institutional Animal
310 Care and Use Committee at the University of California, San Francisco, and the Gladstone
311 Institutes. All precautions were taken to minimize animal stress and reduce the number of animals
312 used.

313

314 ***Mice***
315 We performed all experiments per protocols approved by the Institutional Animal Care and Use
316 Committee at the University of California, San Francisco and Gladstone Institutes. Precautions
317 were taken to minimize stress and the number of animals used in all experiments. Adult (P30–
318 P180) male and female mice were used: wild-type C57BL/6J mice (wild-type, IMSR_JAX:000664;

319   n = 6 mice), Somatostatin (SOM)-Cre mice (SOM-IRES-Cre, IMSR_018973; n = 17 mice),

320   Parvalbumin (PV)-Cre mice (PV-Cre, IMSR_JAX: 017320; C57BL/6 congenic; n = 26 mice),

321   Npas1-Cre-2A-tdTomato BAC transgenic line (NpasCre; RRID:ISMR_JAX:027718; gift from Dr.

322   Aryn Gittis; n = 8 mice). Adult (P30–P180) male and female mice were used: wild-type C57BL/6J

323   (IMSR_JAX:000664; n = 6), Somatostatin (SOM)-Cre (SOM-IRES-Cre, IMSR_018973; n = 17),

324   Parvalbumin (PV)-Cre (IMSR_JAX:017320; C57BL/6 congenic; n = 26), and Npas1-Cre-2A-

325   tdTomato BAC transgenic mice (Npas1-Cre; RRID:IMSR_JAX:027718; gift from Dr. Aryn Gittis;

326   n = 8).

327

328   *Viral injections*

329   We performed viral injections into TRN, VB thalamus, or GPe as described [8,9,28,43,44] in mice aged

330   2–7 months. Briefly, injections using a 10-µl syringe and 34-gauge needle were controlled by

331   pump with a flow rate set to 100 nL/min (World Precision Instruments). **TRN:** 100 nL unilateral

332   injections   of   AAV2/5-EF1a-DIO-hChR2(H134R)-EYFP   (Addgene   plasmid   #20298;

333   RRID:Addgene_20298) at stereotaxic coordinates 1.3–1.6 mm posterior to Bregma, 2.0–2.1 mm

334   lateral, and 2.6–3.4 mm ventral to the cortical surface. **GPe:** 80 nL unilateral injections of the

335   same virus in Npas-Cre mice at –0.28 mm posterior, 2.1 mm lateral, and 4.0 mm ventral from the

336   cortical surface. **VB thalamus:** 200 nL unilateral injections at 1.3–1.6 mm posterior, 1.6–1.7 mm

337   lateral, and 3.0–3.2 mm ventral to the cortical surface.

338

339   *Optogenetic stimulations for whole slice illumination experiments*

340   Optogenetic responses were elicited by activating ChR2-expressing PV-Cre neurons with 450 nm

341   light (OEM Laser Systems, 0.8–2 mW) delivered via a 200-µm optical fiber (Thorlabs) positioned

342   over the TRN (**Supp. Figure 2**).

343

344   *Slice preparation*

345   Thalamic slices were obtained as previously described[8,43]. Mice were euthanized with isoflurane

346   and transcardially perfused with ice-cold sucrose solution (234 mM sucrose, 2.5 mM KCl, 1.25

347   mM NaH2PO4, 10 mM MgSO4, 0.5 mM CaCl2, 26 mM NaHCO3, and 11 mM glucose equilibrated

348   with 95% O_2 and 5% CO_2). Horizontal 250-µm slices containing TRN were cut using a Leica

349   VT1200 microtome (Leica Microsystems). Slices were incubated at 32 °C for 30 min, then

350   recovered for at least 1 h at 24–26 °C in ACSF (126 mM NaCl, 2.5 mM KCl, 1.25 mM NaH_2PO_4,

351   2 mM $MgCl_2$, 2 mM $CaCl_2$, 26 mM $NaHCO_3$, 10 mM glucose) equilibrated with 95% O_2 / 5% CO_2.

352

Patch-clamp electrophysiology

Recordings were performed as previously described[8,43]. TRN neurons were visually identified by differential interference contrast (DIC) optics (Olympus microscope, 63× objective, NA 1.1, WD 1.5 mm; SKU 1-U2M592). Signals were digitized using Axon Digidata 1550 and pClamp 10, and amplified with MultiClamp 700B (Molecular Devices). Recording electrodes (borosilicate glass, Sutter Instruments) had resistances of 2.5–4 MΩ when filled with intracellular solution. Cells were included for analysis if the access resistance was < 25 MΩ, with the exception of one GPe→TRN recipient cell (35 MΩ). Access resistance did not differ between responders (15.6 ± 4.9 MΩ, n = 62 cells) and non-responders (15.9 ± 3.9 MΩ, n = 157 cells; unpaired t-test, p = 0.68). For mapping experiments, the internal solution contained 135 mM CsCl, 10 mM HEPES, 10 mM EGTA, 2 mM $MgCl_2$—$6H_2O$, and 5 mM QX-314 (pH adjusted to 7.3 with CsOH, 290 mOsm). Recordings were performed at room temperature in the presence of kynurenic acid (2 mM; Sigma-Aldrich #K3375) in ACSF. To block $GABA_A$R-mediated currents, gabazine (GBZ; 50 µM; Sigma #SR-95531) prepared in dimethyl sulfoxide (DMSO; Sigma #D8418) was bath-applied.

LASU photostimulation

Optogenetic mapping was performed using the LASU (Laser Applied Stimulation and Uncaging) system (Scientifica, Ltd). This custom-made system includes an epifluorescence SliceScope microscope (Scientifica) with 4× and 63× water-immersion objectives (Olympus) and a uEye camera (IDS). Focal photostimulation used a 405 nm laser. For photostimulation at multiple sites within the field of view, the laser spot was repositioned using a set of two galvanometer scan mirrors controlled by LASU software (v24.1). The laser spot size is estimated to be approximately 1 µm diameter at 63×, and 10 µm diameter at 4×. Laser power, which is controlled by the LASU software, was determined using a power meter, and ranged 0.1–30 mW, with lower powers for GPe→TRN maps (mean 0.4 mW) and higher for intra-TRN maps (mean 3.65 mW). Photostimulation parameters (location, duration, frequency) were defined and saved in LASU software for offline analysis.

Post-hoc imaging

Fixed slices (4% PFA, then 30% sucrose) were imaged using a Zeiss Axio Examiner A1 microscope (GFP and brightfield) to confirm ChR2-EYFP expression. Anatomical landmarks were used to align fixed and live slice images containing the stimulation grid. High-resolution images from Zen software (Zeiss) were used to estimate actual grid dimensions generated by LASU software (LASU v2.1). Specifically, 5 slices with clear alignment between fixed and live slice

13

387   images were used to empirically determine scaling factors, which ranged between 55.5% and
388   70.1%. To ensure a conservative estimation, the lowest scaling factor was used (55.5%) to
389   rescale distance across all experiments. For example, a grid nominally 840 × 180 μm (15 × 4
390   sites, 60 μm spacing) corresponded to a true span of 466.2 × 99.9 μm (33.3 μm spacing) after
391   scaling.

392

393   ***Mapping synaptic connectivity***
394   Voltage-clamp recordings were obtained in Clampex (Molecular Devices) and controlled via LASU
395   software (v24.1). For each cell, mapping was first performed at high magnification (63x objective)
396   to determine the presence or absence of photocurrents and the optimal laser power. Stimulation
397   parameters and grid properties were generated in the LASU software (v24.1). 63x stimulation
398   typically consisted of 160 x 160 μm grids (40 μm spacing) centered around the soma. After
399   determining responses at 63x, the objective was switched to 4x to test connectivity from a larger
400   region of the TRN. 4x stimulation typically consisted of 900 x 240 μm grids (60 μm spacing),
401   although in some cases, the grid spacing and/or shape had to be modified depending on the
402   curvature and thickness of the TRN in the slice. Laser stimulation consisted of 5 ms pulses at
403   each spot, with an inter-pulse-interval of 500-ms (2-Hz) separating consecutive spots, unless
404   otherwise specified. Each trial consisted of each spot being stimulated in a random order; the
405   random order was preserved across trials for each grid. Re-randomization of the stimulation order
406   within the same grid resulted in nearly identical response maps. Coordinates for each point on
407   the stimulation grid, as well as images of the stimulation grid on the slice, were saved for offline
408   analysis. The position of the recorded cell and stimulation grid were reconstructed offline using
409   tiled images of the recorded slice which were cross-registered with higher-resolution bright field
410   and fluorescent images obtained from a Zeiss Axio A1 epifluorescent scope.

411

412   ***Generation of response maps and kinetic analysis of synaptic responses***
413   Response maps were built in Python using the pyABF package and SciPy library. Voltage-clamp
414   recordings obtained in gap-free mode were binned into 520-ms sweeps (including 20-ms
415   preceding the laser pulse) and low-pass Bessel filtered at 500 Hz, with each sweep corresponding
416   to a photostimulation site in a given trial. Sweeps were assigned to the corresponding
417   photostimulation site using the grid coordinates associated with each experiment, which were
418   then used to generate the grid of voltage-clamp responses (e.g., **Figure 2**). The presence of
419   eIPSCs was determined for each photostimulation site and trial (for each experiment) by two
420   investigators. The inclusion criteria for eIPSCs was as follows: an inward (negative) current with

14

421   amplitude greater than 10 pA, asymmetric rise and decay (i.e., fast rise, slow decay), occurring

422   after 5 ms from laser onset and within 50 ms from laser offset. A given photostimulation site was

423   considered a "hot spot" if it contained at least 2 trials with an evoked synaptic current with

424   consistent onset latency (within 10 ms of each other) and did not contain a spontaneously

425   occurring IPSC preceding the laser onset. This manual curation was used to generate a "masking

426   file" for each experiment, which was used in conjunction with the SciPy find_peaks function, to

427   identify the amplitude of synaptic currents at photostimulation sites and trials containing eIPSCs.

428   The find_peaks function (parameters: prominence=2, threshmax=10000) was used to extract only

429   the amplitude, which was visually cross-validated against raw traces. The orientation of response

430   maps were aligned to the mouse brain atlas (anterior/posterior, medial/lateral). The distance

431   between the stimulation site and somatic recording site was estimated by approximating the

432   location of the recording pipette tip on the stimulation grid to within 2 to 4 sites. eIPSCs identified

433   above were analyzed separately in Clampfit (Molecular Devices) to automatically extract half-

434   width, decay time, area and amplitude, and manually extract rise time and latency. All events

435   imported into Clampfit were manually validated to be eIPSCs to exclude spontaneously occurring

436   IPSCs or artifacts. Kinetic analyses presented in **Figure 1** include eIPSCs observed at the

437   maximally active photostimulation site for a given cell, while analyses presented in **Figure 2**

438   include all eIPSCs detected across all photostimulation sites. In **Figure 2I** and **Supp. Figure 2C**,

439   comparison was performed only for responder cells which were mapped at low magnification.

440   Maps were typically obtained using a 15 x 4 grid (60 μm spacing).

441

442   ***Current-clamp analysis***

443   Data were analyzed in Clampfit (Molecular Devices). We determined the following epochs per

444   trial for analysis: baseline (200 ms preceding laser pulse), laser (30ms starting at laser onset for

445   square pulses, and 100 ms for ramp pulses), post-laser (200 ms following laser epoch), and

446   recovery (200 ms following post-laser). Current injection duration was 2 s. Mean firing rates were

447   calculated per epoch (spikes / epoch duration) and averaged across trials.

448   Firing-rate histograms (**Figure 2E**) were binned at 10 ms and normalized by trial count.

449   For statistical analyses (**Figure 2G–H**), only matched samples were included.

450   Each cell's mean firing rate (or baseline-normalized rate) in laser vs. no-laser conditions was

451   compared using paired or ratio-paired t-tests.

452

459

460 **Author Contributions:** Conceptualization: JTP, JRH. Methodology: FSC, JRH, JTP.

461 Investigation: FSC, JTP. Data curation: FSC, JTP. Analysis: FSC, JTP. Visualization: FSC, JTP,

462 Supervision: JTP, JRH. Funding acquisition: FSC, JRH, JTP. Writing – original draft: FSC, JTP.

463 Writing – reviewing & editing: all authors.

References

1. Fogerson, P.M., and Huguenard, J.R. (2016). Tapping the Brakes: Cellular and Synaptic Mechanisms that Regulate Thalamic Oscillations. Neuron *92*, 687–704. https://doi.org/10.1016/j.neuron.2016.10.024.

2. Jones, E.G. (1985). Principles of Thalamic Organization. In The Thalamus, E. G. Jones, ed. (Springer US), pp. 85–149. https://doi.org/10.1007/978-1-4615-1749-8_3.

3. Lee, S.-H., Govindaiah, G., and Cox, C.L. (2007). Heterogeneity of firing properties among rat thalamic reticular nucleus neurons. J Physiol *582*, 195–208. https://doi.org/10.1113/jphysiol.2007.134254.

4. Crabtree, J.W. (2018). Functional Diversity of Thalamic Reticular Subnetworks. Front Syst Neurosci *12*, 41. https://doi.org/10.3389/fnsys.2018.00041.

5. Halassa, M.M., Chen, Z., Wimmer, R.D., Brunetti, P.M., Zhao, S., Zikopoulos, B., Wang, F., Brown, E.N., and Wilson, M.A. (2014). State-dependent architecture of thalamic reticular subnetworks. Cell *158*, 808–821. https://doi.org/10.1016/j.cell.2014.06.025.

6. Halassa, M.M., and Acsády, L. (2016). Thalamic Inhibition: Diverse Sources, Diverse Scales. Trends Neurosci *39*, 680–693. https://doi.org/10.1016/j.tins.2016.08.001.

7. Jones, E.G. (1975). Some aspects of the organization of the thalamic reticular complex. J Comp Neurol *162*, 285–308. https://doi.org/10.1002/cne.901620302.

8.   Clemente-Perez, A., Makinson, S.R., Higashikubo, B., Brovarney, S., Cho, F.S., Urry, A., Holden, S.S., Wimer, M., Dávid, C., Fenno, L.E., et al. (2017). Distinct Thalamic Reticular Cell Types Differentially Modulate Normal and Pathological Cortical Rhythms. Cell Rep *19*, 2130–2142. https://doi.org/10.1016/j.celrep.2017.05.044.

9.   Hoseini, M.S., Higashikubo, B., Cho, F.S., Chang, A.H., Clemente-Perez, A., Lew, I., Ciesielska, A., Stryker, M.P., and Paz, J.T. (2021). Gamma rhythms and visual information in mouse V1 specifically modulated by somatostatin+ neurons in reticular thalamus. Elife *10*, e61437. https://doi.org/10.7554/eLife.61437.

10.   Martinez-Garcia, R.I., Voelcker, B., Zaltsman, J.B., Patrick, S.L., Stevens, T.R., Connors, B.W., and Cruikshank, S.J. (2020). Two dynamically distinct circuits drive inhibition in the sensory thalamus. Nature *583*, 813–818. https://doi.org/10.1038/s41586-020-2512-5.

11.   Li, Y., Lopez-Huerta, V.G., Adiconis, X., Levandowski, K., Choi, S., Simmons, S.K., Arias-Garcia, M.A., Guo, B., Yao, A.Y., Blosser, T.R., et al. (2020). Distinct subnetworks of the thalamic reticular nucleus. Nature *583*, 819–824. https://doi.org/10.1038/s41586-020-2504-5.

12.   Hazrati, L.N., and Parent, A. (1991). Projection from the external pallidum to the reticular thalamic nucleus in the squirrel monkey. Brain Res *550*, 142–146. https://doi.org/10.1016/0006-8993(91)90418-u.

13.   Paz, J.T., and Huguenard, J.R. (2015). Microcircuits and their interactions in epilepsy: is the focus out of focus? Nat Neurosci *18*, 351–359. https://doi.org/10.1038/nn.3950.

14.   Landisman, C.E., Long, M.A., Beierlein, M., Deans, M.R., Paul, D.L., and Connors, B.W. (2002). Electrical synapses in the thalamic reticular nucleus. J Neurosci *22*, 1002–1009. https://doi.org/10.1523/JNEUROSCI.22-03-01002.2002.

15.   Long, M.A., Landisman, C.E., and Connors, B.W. (2004). Small clusters of electrically coupled neurons generate synchronous rhythms in the thalamic reticular nucleus. J Neurosci *24*, 341–349. https://doi.org/10.1523/JNEUROSCI.3358-03.2004.

16.   Deleuze, C., and Huguenard, J.R. (2006). Distinct electrical and chemical connectivity maps in the thalamic reticular nucleus: potential roles in synchronization and sensation. J Neurosci *26*, 8633–8645. https://doi.org/10.1523/JNEUROSCI.2333-06.2006.

17. Beenhakker, M.P., and Huguenard, J.R. (2009). Neurons that fire together also conspire together: is normal sleep circuitry hijacked to generate epilepsy? Neuron *62*, 612–632. https://doi.org/10.1016/j.neuron.2009.05.015.

18. Shu, Y., and McCormick, D.A. (2002). Inhibitory interactions between ferret thalamic reticular neurons. J Neurophysiol *87*, 2571–2576. https://doi.org/10.1152/jn.00850.2001.

19. Makinson, C.D., Tanaka, B.S., Sorokin, J.M., Wong, J.C., Christian, C.A., Goldin, A.L., Escayg, A., and Huguenard, J.R. (2017). Regulation of Thalamic and Cortical Network Synchrony by Scn8a. Neuron *93*, 1165-1179.e6. https://doi.org/10.1016/j.neuron.2017.01.031.

20. Parker, P.R.L., Cruikshank, S.J., and Connors, B.W. (2009). Stability of electrical coupling despite massive developmental changes of intrinsic neuronal physiology. J Neurosci *29*, 9761–9770. https://doi.org/10.1523/JNEUROSCI.4568-08.2009.

21. Cruikshank, S.J., Urabe, H., Nurmikko, A.V., and Connors, B.W. (2010). Pathway-specific feedforward circuits between thalamus and neocortex revealed by selective optical stimulation of axons. Neuron *65*, 230–245. https://doi.org/10.1016/j.neuron.2009.12.025.

22. Hou, G., Smith, A.G., and Zhang, Z.-W. (2016). Lack of Intrinsic GABAergic Connections in the Thalamic Reticular Nucleus of the Mouse. J Neurosci *36*, 7246–7252. https://doi.org/10.1523/JNEUROSCI.0607-16.2016.

23. Hernández, V.M., Hegeman, D.J., Cui, Q., Kelver, D.A., Fiske, M.P., Glajch, K.E., Pitt, J.E., Huang, T.Y., Justice, N.J., and Chan, C.S. (2015). Parvalbumin+ Neurons and Npas1+ Neurons Are Distinct Neuron Classes in the Mouse External Globus Pallidus. J Neurosci *35*, 11830–11847. https://doi.org/10.1523/JNEUROSCI.4672-14.2015.

24. Lee, J.-H., Latchoumane, C.-F.V., Park, J., Kim, J., Jeong, J., Lee, K.-H., and Shin, H.-S. (2019). The rostroventral part of the thalamic reticular nucleus modulates fear extinction. Nat Commun *10*, 4637. https://doi.org/10.1038/s41467-019-12496-9.

25. Fernandez, L.M., Vantomme, G., Osorio-Forero, A., Cardis, R., Béard, E., and Lüthi, A. (2018). Thalamic reticular control of local sleep in mouse sensory cortex. eLife *7*, e39111. https://doi.org/10.7554/eLife.39111.

26. Ahrens, S., Jaramillo, S., Yu, K., Ghosh, S., Hwang, G.-R., Paik, R., Lai, C., He, M., Huang, Z.J., and Li, B. (2015). ErbB4 regulation of a thalamic reticular nucleus circuit for sensory selection. Nat Neurosci *18*, 104–111. https://doi.org/10.1038/nn.3897.

27.   Jang, S.-S., Agranonik, N., and Huguenard, J.R. (2025). Actions of the antiseizure drug carbamazepine in the thalamic reticular nucleus: Potential mechanism of aggravating absence seizures. Proc Natl Acad Sci U S A *122*, e2500644122. https://doi.org/10.1073/pnas.2500644122.

28.   Paz, J.T., Bryant, A.S., Peng, K., Fenno, L., Yizhar, O., Frankel, W.N., Deisseroth, K., and Huguenard, J.R. (2011). A new mode of corticothalamic transmission revealed in the Gria4(-/-) model of absence epilepsy. Nat Neurosci *14*, 1167–1173. https://doi.org/10.1038/nn.2896.

29.   Klausberger, T., and Somogyi, P. (2008). Neuronal Diversity and Temporal Dynamics: The Unity of Hippocampal Circuit Operations. Science *321*, 53–57. https://doi.org/10.1126/science.1149381.

30.   Lovett-Barron, M., Turi, G.F., Kaifosh, P., Lee, P.H., Bolze, F., Sun, X.-H., Nicoud, J.-F., Zemelman, B.V., Sternson, S.M., and Losonczy, A. (2012). Regulation of neuronal input transformations by tunable dendritic inhibition. Nat Neurosci *15*, 423–430. https://doi.org/10.1038/nn.3024.

31.   Landisman, C.E., and Coulon, P. (2024). A mixed electrical and chemical synapse in the thalamic reticular nucleus. J Neurophysiol *132*, 1955–1963. https://doi.org/10.1152/jn.00339.2024.

32.   Picardo, M.A., Guigue, P., Bonifazi, P., Batista-Brito, R., Allene, C., Ribas, A., Fishell, G., Baude, A., and Cossart, R. (2011). Pioneer GABA cells comprise a subpopulation of hub neurons in the developing hippocampus. Neuron *71*, 695–709. https://doi.org/10.1016/j.neuron.2011.06.018.

33.   Sohal, V.S., and Huguenard, J.R. (2003). Inhibitory interconnections control burst pattern and emergent network synchrony in reticular thalamus. J Neurosci *23*, 8978–8988. https://doi.org/10.1523/JNEUROSCI.23-26-08978.2003.

34.   Coulon, P., and Landisman, C.E. (2017). The Potential Role of Gap Junctional Plasticity in the Regulation of State. Neuron *93*, 1275–1295. https://doi.org/10.1016/j.neuron.2017.02.041.

35.   Taube, J.S. (2007). The head direction signal: origins and sensory-motor integration. Annu Rev Neurosci *30*, 181–207. https://doi.org/10.1146/annurev.neuro.29.051605.112854.

36.   Couey, J.J., Witoelar, A., Zhang, S.-J., Zheng, K., Ye, J., Dunn, B., Czajkowski, R., Moser, M.-B., Moser, E.I., Roudi, Y., et al. (2013). Recurrent inhibitory circuitry as a mechanism for grid formation. Nat Neurosci *16*, 318–324. https://doi.org/10.1038/nn.3310.

37.   Huntsman, M.M., Porcello, D.M., Homanics, G.E., DeLorey, T.M., and Huguenard, J.R. (1999). Reciprocal inhibitory connections and network synchrony in the mammalian thalamus. Science *283*, 541–543. https://doi.org/10.1126/science.283.5401.541.

38.   Holden, S.S., Grandi, F.C., Aboubakr, O., Higashikubo, B., Cho, F.S., Chang, A.H., Forero, A.O., Morningstar, A.R., Mathur, V., Kuhn, L.J., et al. (2021). Complement factor C1q mediates sleep spindle loss and epileptic spikes after mild brain injury. Science *373*, eabj2685. https://doi.org/10.1126/science.abj2685.

39.   Jang, S.-S., Takahashi, F., and Huguenard, J.R. (2025). Reticular thalamic hyperexcitability drives autism spectrum disorder behaviors in the Cntnap2 model of autism. Science Advances *11*, eadw4682. https://doi.org/10.1126/sciadv.adw4682.

40.   Wells, M.F., Wimmer, R.D., Schmitt, L.I., Feng, G., and Halassa, M.M. (2016). Thalamic reticular impairment underlies attention deficit in Ptchd1(Y/-) mice. Nature *532*, 58–63. https://doi.org/10.1038/nature17427.

41.   Herrera, C.G., Cadavieco, M.C., Jego, S., Ponomarenko, A., Korotkova, T., and Adamantidis, A. (2016). Hypothalamic feedforward inhibition of thalamocortical network controls arousal and consciousness. Nat Neurosci *19*, 290–298. https://doi.org/10.1038/nn.4209.

42.   Crick, F. (1984). Function of the thalamic reticular complex: the searchlight hypothesis. Proc Natl Acad Sci U S A *81*, 4586–4590. https://doi.org/10.1073/pnas.81.14.4586.

43.   Ritter-Makinson, S., Clemente-Perez, A., Higashikubo, B., Cho, F.S., Holden, S.S., Bennett, E., Chkhaidze, A., Eelkman Rooda, O.H.J., Cornet, M.-C., Hoebeek, F.E., et al. (2019). Augmented Reticular Thalamic Bursting and Seizures in Scn1a-Dravet Syndrome. Cell Rep *26*, 54-64.e6. https://doi.org/10.1016/j.celrep.2018.12.018.

44.   Abecassis, Z.A., Berceau, B.L., Win, P.H., García, D., Xenias, H.S., Cui, Q., Pamukcu, A., Cherian, S., Hernández, V.M., Chon, U., et al. (2020). Npas1+-Nkx2.1+ Neurons Are an Integral Part of the Cortico-pallido-cortical Loop. J Neurosci *40*, 743–768. https://doi.org/10.1523/JNEUROSCI.1199-19.2019.

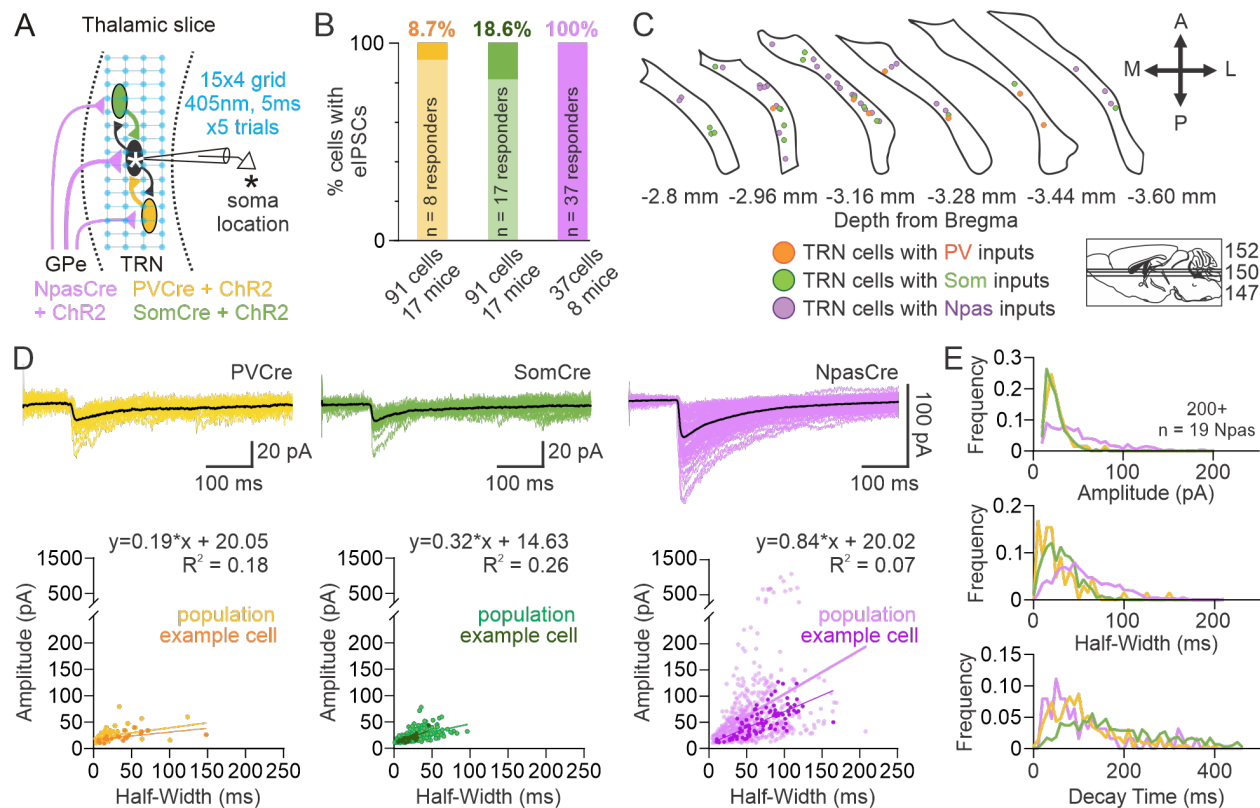45.   The Mouse Brain in Stereotaxic Coordinates, Compact (2008).

Figure 1

Figure 1. TRN neurons receive GABAergic synaptic inputs from intra-TRN and external globus pallidus

A. Schematic of focal photostimulation. AAV2/5-DIO-ChR2-eYFP was injected into the TRN of PV-Cre or Som-Cre mice, and into the GPe of Npas-Cre mice. Whole-cell voltage-clamp recordings were obtained from TRN neurons while ChR2-expressing axons were focally stimulated in a 15 × 4 grid (spanning 460 × 100 μm) along the anterior-posterior and medial-lateral axes of the TRN. The asterisk * indicates the location of the recorded cell body. At each site, a 5 ms, 405 nm laser pulse was delivered. Stimulation sites were activated in randomized order at 2 Hz (one site every 0.5 s).

B. Proportion of TRN neurons showing evoked inhibitory postsynaptic currents (eIPSCs) in response to activation of TRN^{PV}, TRN^{SOM}, or GPe^{NPas} inputs. n = 8 of 91 cells from 17 PV-Cre mice; n = 17 of 91 cells from 17 Som-Cre mice; n = 37 of 37 cells from 8 Npas-Cre mice.

C. Location of postsynaptic TRN cells responding to TRN^{PV}, TRN^{SOM}, or GPe^{Npas} inputs in the dorsal-ventral horizontal plane. Brain schematic adapted from [45].

21

478   **D.** Representative TRN eIPSCs recorded at –70 mV in response to optogenetic activation of PV,

479   Som, or Npas synaptic inputs. Black traces indicate averages of all synaptic events from each

480   cell; gray traces show individual events. Scatter plots (bottom) show eIPSC's half-width (time to

481   50% decay from peak) versus amplitude. Each point represents an individual eIPSC. PV-triggered

482   eIPSCs: n = 65 events from 4 cells; Som-triggered eIPSCs: n = 232 events from 13 cells; Npas-

483   triggered eIPSCs: n = 635 events from 15 cells.

484   **E.** Relative frequency histograms of eIPSC amplitude (5 pA bins), half-width (5 ms bins), and

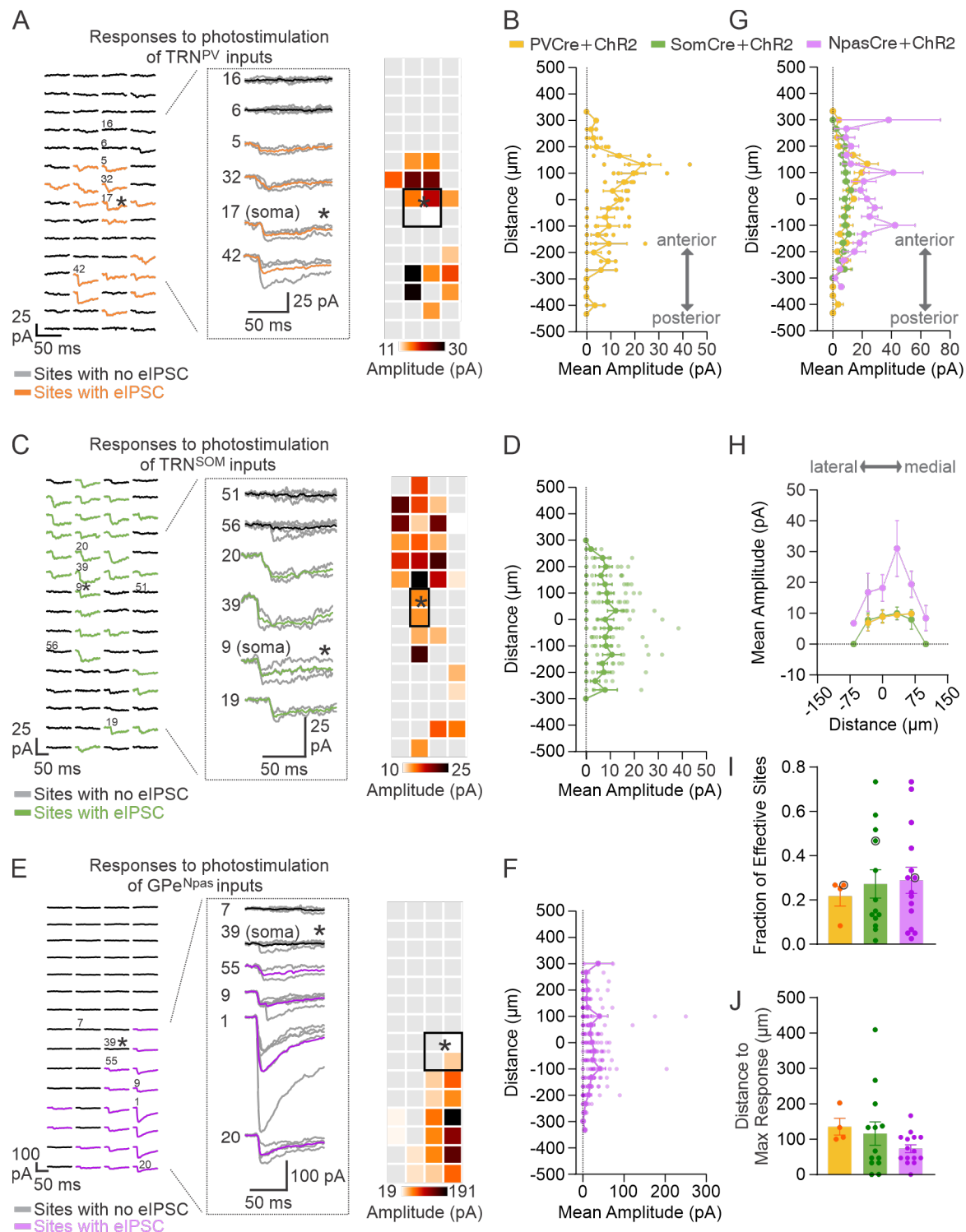485   decay time (10 ms bins).

Figure 2

Figure 2. Spatial Distribution of Inhibitory Synaptic Inputs to TRN

A. Example photostimulation responses from a TRN^PV-recipient TRN neuron obtained from a PV-Cre mouse expressing AAV2/5-DIO-ChR2-eYFP in TRN. Left: voltage-clamp recordings from a

489   TRN cell held at –70 mV demonstrating the spatial distribution of monosynaptic GABAergic inputs

490   upon optogenetic activation of PV+ inputs. The response map shows eIPSCs averaged across

491   trials at each site between –20 and +200 ms relative to laser onset. A site was considered a "hot

492   spot" (orange) if activation evoked eIPSCs $\geq$ 10 pA on ≥2 trials with event onset jitter ≤10 ms, with

493   no spontaneous IPSC immediately preceding the laser onset. Nonresponsive sites (black traces)

494   are averaged across all trials; "hot spots" (orange traces) are averaged across trials containing

495   eIPSCs. Inset: sites labeled on the grid (left) are expanded (right), showing individual trials (grey)

496   and the average (orange). Numbers indicate stimulation order. Right: heatmap of eIPSC

497   amplitudes from 16 "hot spots" (of 60 sites), averaged across 6 trials. Grey indicates

498   nonresponsive sites. The recorded cell body is indicated by the black square.

499   **B.** Spatial distribution and mean amplitude of eIPSCs evoked by activation of *PV+* inputs along

500   the anterior-posterior axis of the TRN. Data represent mean ± SEM from n = 4 responsive cells.

501   **C–D.** Same as in (A–B), but from a TRN^{SOM}-recipient TRN neuron recorded from a Som-Cre

502   mouse expressing ChR2 in the TRN. "Hot spots" shown in green. Example heatmap shows

503   eIPSCs from 28 "hot spots" averaged across 5 trials from one cell. Data in (D) represent mean ±

504   SEM from n = 9 responsive cells.

505   **E–F.** Same as in (A–B), but from a GPe^{Npas}-recipient TRN neuron recorded from an Npas1-Cre

506   mouse expressing ChR2 in GPe. "Hot spots" shown in purple. Example heatmap shows eIPSCs

507   from 18 "hot spots" averaged across 5 trials from one cell. Data in (F) represent mean ± SEM

508   from n = 14 responsive cells.

509   **G.** Anterior-posterior distribution of the amplitude of eIPSCs mapped from PV, Som, or Npas

510   inputs onto TRN neurons (mean $\pm$ SEM), averaged across rows using one map per cell. Distance

511   is shown relative to the recorded cell. Maps were generated using a 15 × 4 grid (33 µm spacing)

512   for 25 of 27 cells; two PV maps used 20 × 3 grids (33 µm spacing). PV maps: n = 4 cells; Som

513   maps: n = 9 cells; Npas maps: n = 14 cells.

514   **H.** Medial-lateral distribution of the amplitude of eIPSCs mapped from PV, Som, or Npas inputs

515   onto TRN neurons, averaged across columns using one map per cell (mean $\pm$ SEM).

516   **I.** Fraction of "hot spots" (photostimulation sites evoking synaptic responses), obtained by

517   stimulating PV, Som, or Npas fibers in TRN. PV maps: n = 4 cells (3 mice); Som maps: n = 13

518   cells (9 mice), Npas maps: n = 15 cells (5 mice). One map from one cell was included in this

519   analysis. Plots show mean ± SEM. Kruskal-Wallis test, not significant (p = 0.949; p = 0.96).

520   **J.** Distance from recorded cell to site of maximal (trial-averaged) eIPSC amplitude in each map.
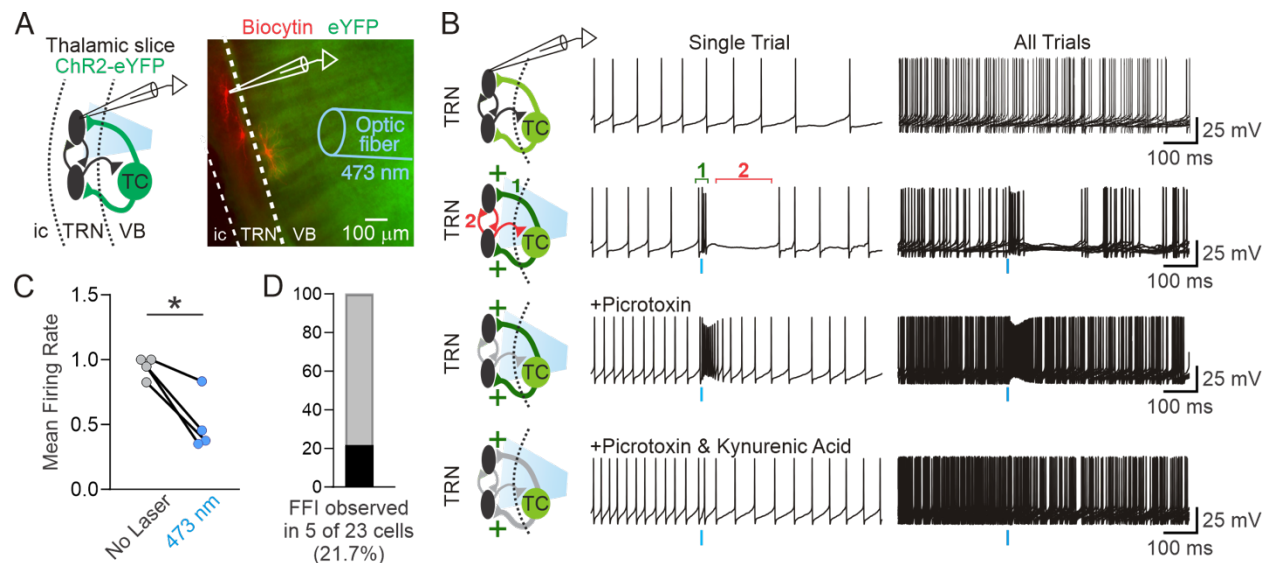
Figure 3

Figure 3. Feed-forward inhibition within the TRN generated by activation of ventrobasal thalamocortical axons in TRN
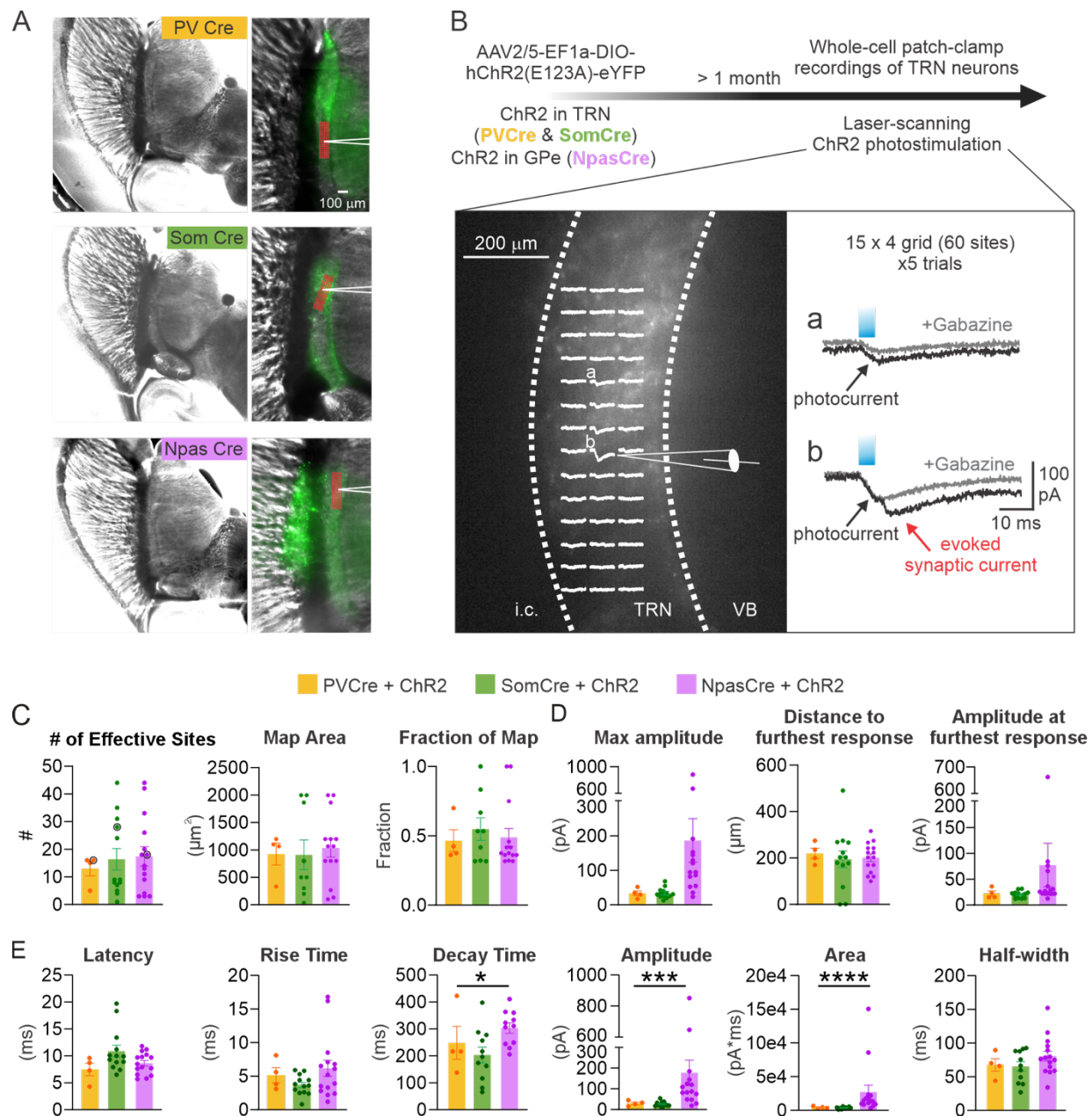
A. Schematic (left) and fluorescent image (right) showing ChR2 expression in thalamocortical (TC) neurons of the ventrobasal (VB) thalamus in adult mice. Whole-cell current-clamp recordings were performed from TRN neurons in horizontal thalamic slices, and 473 nm light pulses were delivered through an optical fiber positioned above the slice. Representative fluorescent image shows ChR2 (eYFP, green) expression and biocytin-filled TRN neurons (red).

B. Example membrane potential trace from a TRN neuron. A 1 ms pulse of blue light evokes a transient depolarization followed by a pause in firing.

C. Decrease in TRN firing rate relative to baseline following optogenetic activation of ChR2-expressing VB axons in TRN, indicating feed-forward inhibition. n = 4 cells. Data passed the Shapiro-Wilk normality test ($p > 0.05$); paired t-test on matched samples (*$p = 0.02$).

D. Proportion of TRN neurons in which TC-TRN-TRN feed-forward inhibition was observed (n = 5 of 23 cells, 4 mice).

25

Supplemental Figure 1

Supplemental Figure 1. Characterization of optogenetic mapping and spatial organization of GABAergic inputs to TRN neurons. Related to Figures 1, 2.

A. Brightfield and fluorescent images of horizontal thalamic slices (2.5x magnification, left; 5x magnification, right) from PV-Cre and Som-Cre mice injected with AAV2/5-DIO-ChR2-eYFP (green) into TRN, and from an Npas-Cre mouse injected with the same viral construct into GPe. Right: example showing the position of the recording pipette and the optogenetic stimulation grid (red).
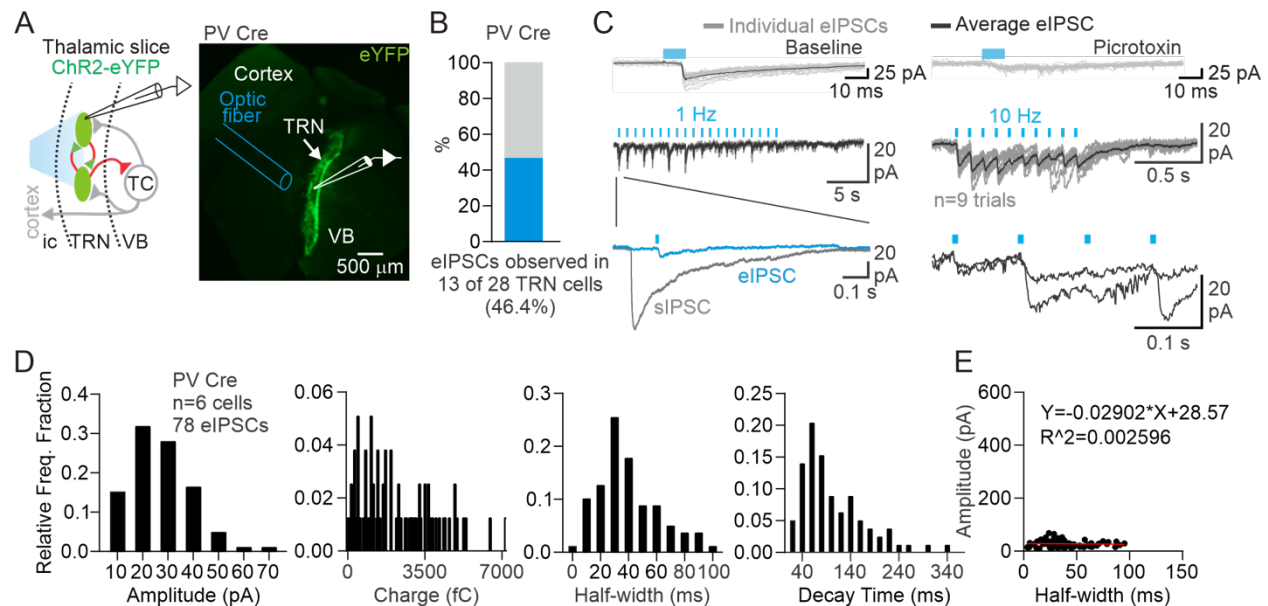
26

542   **B.** Overview of the photostimulation experiment. Inset shows a brightfield image of TRN

543   expressing ChR2 in a PV-Cre mouse. Average responses from focal photostimulation at each site

544   in the 15 x 4 grid are overlaid on the slice image from one recorded TRN neuron. (a) indicates a

545   site evoking only a photocurrent, visible immediately upon the laser pulse and unchanged by

546   Gabazine application. (b) indicates a site evoking both a photocurrent and a delayed inward

547   current (eIPSC), which is selectively abolished by Gabazine.

548   **C.** Extent of synaptic connectivity from neurochemically and anatomically distinct sources of

549   GABAergic input. Number of "hot spots" (effective photostimulation sites) obtained by stimulating

550   TRN^{PV}, TRN^{SOM}, or GPe^{Npas} fibers onto postsynaptic TRN neurons (left). PV maps: n = 4 cells (3

551   mice); Som maps: n = 13 cells (9 mice), Npas maps: n = 15 cells (5 mice). One map from one cell

552   was included in this analysis. Bar graphs show mean ± SEM. Kruskal–Wallis test, not significant

553   ($p = 0.949$; $p = 0.96$). Area representing the anterior–posterior and medial–lateral extent of

554   responses ("map area") (center) and the fraction of responsive sites within this area (right).

555   **D.** Amplitude of the site of maximal, trial-averaged eIPSC response (left), distance from the

556   recorded cell to the most distal eIPSC response (center), and trial-averaged eIPSC amplitude at

557   that site (right).

558   **E.** Properties of eIPSCs recorded at the maximal responsive site for each map. PV: n = 4 cells;

559   Som: n = 13 cells; Npas: n = 15 cells. **Kruskal–Wallis test, $p < 0.05$, **$p < 0.0005$, *$p < 0.00005$.

Supplemental Figure 2

Supplemental Figure 2. Optogenetic activation of intra-TRN GABAergic synapses in PV-Cre mice. Related to Figure 1.

A. Schematic (left) and fluorescent image (right) of a horizontal thalamic slice from a PV-Cre mouse expressing ChR2 in TRN (AAV injection into the TRN). Whole-cell voltage-clamp recordings were performed from TRN neurons, while an optical fiber delivered 473 nm light pulses to activate ChR2- or ChETA-expressing axons (not shown).
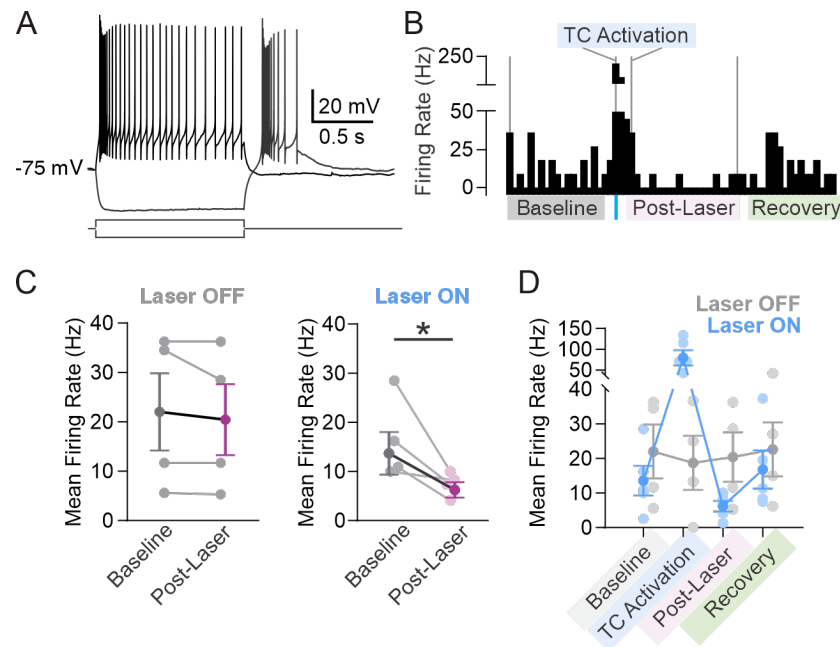
B. Top: example synaptic currents evoked by ChR2 activation, blocked by picrotoxin. Middle: eIPSCs reliably entrained at 1 Hz and 10 Hz stimulation.

C. Fraction of TRN cells showing eIPSCs following wider-field (200 um) photoactivation of TRN^{PV} inputs (n = 13 of 28 cells; ChETA).

D. Kinetic properties of eIPSCs evoked by TRN^{PV} activation. Distributions of amplitude, charge, half-width, and decay time (n = 78 eIPSCs from 6 cells).

E. Relationship between eIPSC half-width and amplitude.

Supplemental Figure 3

Supplemental Figure 3. Optogenetic activation transiently suppresses TRN neuron firing. Related to Figure 3.

A. Representative whole-cell current-clamp traces of a TRN neuron in response to depolarizing and hyperpolarizing current steps.

B. Firing rate of example TRN neuron exhibiting feed-forward inhibition upon activation of ventrobasal thalamocortical axons (same as in **Figure 3B**). A 1 ms blue light pulse triggers a brief increase followed by suppression of firing. Vertical lines indicate analysis epochs: baseline (200 ms), laser (30 ms), post-laser (200 ms), and recovery (200 ms).

C. Light-evoked suppression of firing rate observed with ChR2-activation (right) but not during no-laser control trials (left). n = 4 cells. Data passed the Shapiro–Wilk normality test ($p > 0.05$). Ratio paired t-test: no laser, $p = 0.27$ (ns); 473 nm, $*p = 0.032$. Same data shown in Figure 3C.

D. Mean firing rate across epochs in responder cells (n = 5) with (blue) and without (grey) laser stimulation. Two-way repeated-measures ANOVA: interaction, $***p < 0.0001$; time, $*p = 0.0121$; laser, $p = 0.21$ (ns); subject, $p = 0.21$ (ns).